

## Article

# Comparison of Coupled Model Intercomparison Project Phases 5 and 6 in Simulating Diurnal Cloud Cycle

Zhiye Jiang<sup>1,2</sup>, Yahan An<sup>1,2</sup> and Jun Yin<sup>1,2,\*</sup>

<sup>1</sup> Key Laboratory of Hydrometeorological Disaster Mechanism and Warning of Ministry of Water Resources (HYMED)/CIC-FEMD, Nanjing University of Information Science and Technology, Nanjing 210044, China; 20211260001@nuist.edu.cn (Z.J.); 202212600004@nuist.edu.cn (Y.A.)

<sup>2</sup> School of Hydrology and Water Resources, Nanjing University of Information Science and Technology, Nanjing 210044, China

\* Correspondence: jun.yin@nuist.edu.cn

**Abstract:** Cloud dynamics and their response to future climate change continue to present a significant source of uncertainty in climate predictions. Besides the average cloud properties, the diurnal cloud cycle (DCC) exerts a substantial influence on Earth's energy balance by reflecting solar radiation during the daytime and continuously absorbing and reemitting longwave radiation throughout the whole day. Previous studies have demonstrated that climate models exhibit certain discrepancies in simulating the DCC; however, less research attention has been paid to the patterns of these DCC biases and their impacts on modeling the Earth's energy balance. Here, we employ satellite data to compare DCC patterns in Coupled Model Intercomparison Project Phase 5 (CMIP5) and their latest versions in CMIP6 at both regional and global scales. We found that some of the latest climate models tend to have larger DCC biases when using satellite observations as the references, and the radiative effects due to DCC changes account for nearly 50% of the changes in total cloud radiative effects (CREs), suggesting that the DCC biases play a significant role in modeling the global energy budget. We therefore call for improving cloud parameterization schemes with particular attention to their diurnal cycle to reduce their impacts on future climate projections.

**Keywords:** CMIP5; CMIP6; diurnal cloud cycle; cloud radiative effects; atmospheric convection



**Citation:** Jiang, Z.; An, Y.; Yin, J. Comparison of Coupled Model Intercomparison Project Phases 5 and 6 in Simulating Diurnal Cloud Cycle. *Atmosphere* **2024**, *15*, 381. <https://doi.org/10.3390/atmos15030381>

Academic Editor: Alexander V. Chernokulsky

Received: 14 February 2024

Revised: 11 March 2024

Accepted: 17 March 2024

Published: 20 March 2024



**Copyright:** © 2024 by the authors. Licensee MDPI, Basel, Switzerland. This article is an open access article distributed under the terms and conditions of the Creative Commons Attribution (CC BY) license (<https://creativecommons.org/licenses/by/4.0/>).

## 1. Introduction

Modeling clouds and their response to global warming is still one of the largest sources of uncertainties in projecting future climate [1–3]. Specifically, the timing of clouds can modulate Earth's energy balance because daytime clouds can reflect solar radiation but nighttime clouds keep the thermal radiation, showing contrasting effects on the global temperature [4]. The presence of clouds at different times of the day, often referred to as the diurnal cloud cycle (DCC), has recently received much research attention [5–8]. Most of these studies found biases in DCC simulation particularly over the land [2], where the atmospheric convection and cloud dynamics can be strongly controlled by surface heat flux [9–11]. This land–atmosphere interaction is particularly difficult to simulate as the small-scale convective physics is not explicitly represented in climate models [12], possibly contributing to the uncertainties in climate projections [4].

Moreover, the DCC also seems to shift in response to global warming, thus potentially playing a significant role in controlling future climate [6,13]. In response to global warming, hydrological process, atmospheric stability, and vegetation may experience certain changes [2,14], thus influencing the atmospheric convection and possibly shifting the DCC [14–16]. This forms a critical feedback loop and could be one of the significant components of the overall cloud radiative effects (CREs). It has been found that the difference between daytime and nighttime cloud fraction is strongly correlated with the Pacific decadal oscillation (PDO) [6], an important indicator of large-scale circulation [17]. It is

also found that the changes in the diurnal cycle of tropical high clouds are in agreement with the trends of the global mean temperature [13]. Given its strong impacts on Earth's energy balance, the DCC may play a significant role in modulating future climate.

While some studies show changes in DCC simulation in the latest climate models [7], limited information has been offered regarding its impacts on Earth's energy balance and its role in adjusting climate sensitivity, a key metric measuring the global temperature increase response to a doubling of atmospheric carbon dioxide concentration. It has been reported that the latest CMIP6 models have the largest variations in climate sensitivity, ranging from 1.8 to 5.6 °C, which may be associated with the large inter-model spread of CREs [2,18–20]. While great efforts have been devoted to deciphering the key cloud features in controlling climate projections, less attention has been paid to the DCC changes, which may offer new insight into our understanding of the uncertainties in climate projections.

Towards this goal, here we compared the DCCs from both the CMIP5 and CMIP6 models and paid particular attention to their radiative effects. We found that the DCC tends to shift in the same direction with the same order of magnitude over the land and ocean in most climate models from CMIP5 to CMIP6. The radiative effects of these DCC changes are nearly half of these impacts from the changes of all cloud properties, highlighting the critical role of the timing of clouds in modulating the Earth's energy balance and possibly influencing climate projections. The paper is organized as follows: Section 2 introduces the data and methods used in this study, including the evaluation of the DCC phase and the quantification of its radiation effects; Section 3 compares the DCC at regional and global scales and discusses its impacts on global energy balance, and conclusions are summarized in Section 4.

## 2. Data and Methods

To make a one-to-one comparison, we used the three-hourly total cloud fraction (variable name: clt) from 12 climate models, including 6 from CMIP5 and the corresponding upgraded versions from CMIP6. It should be noted that not all institutions provide model outputs at high temporal resolutions in both CMIP5 and CMIP6. Table 1 summarizes the model names as well as the institutions and spatial resolutions. To compare with satellite products of cloud fraction in recent years, we focused on the “historical” experiments [21]. We selected the ensemble ‘r1i1p1’ from CMIP5 and the similar ensemble of ‘r1i1p1f1’ from CMIP6 but used others if these ensembles were not available. In the CMIP project, some ensemble documentation is harvested by ES-DOC from published netCDF files, but additional information will be available in ES-DOC. In each model output file, the ‘ripf’ identifier (‘rip’ identifier for CMIP5) is used to uniquely distinguish each member of an ensemble, ‘r’ for realization, ‘i’ for initialization, ‘p’ for physics, and ‘f’ for forcing.

**Table 1.** Summary of the climate models used for comparison.

Institute	Model Name	CMIP	Res.
CMCC	CMCC-CM	5	$1.33^\circ \times 0.75^\circ$
	CMCC-CM2-SR5	6	$1.25^\circ \times 0.94^\circ$
CNRM-CERFACS	CNRM-CM5	5	$1.41^\circ \times 1.41^\circ$
	CNRM-CM6-1	6	$1.41^\circ \times 1.41^\circ$
LASG-CESS	FGOALS-g2	5	$2.81^\circ \times 3.00^\circ$
CAS	FGOALS-g3	6	$2.00^\circ \times 2.25^\circ$
NOAA-GFDL	GFDL-CM3	5	$2.5^\circ \times 2.00^\circ$
	GFDL-CM4	6	$1.25^\circ \times 1.00^\circ$
MOHC	HadGEM2-ES	5	$1.875^\circ \times 1.25^\circ$
	HadGEM3-GC31-LL	6	$1.875^\circ \times 1.25^\circ$
IPSL	IPSL-CM5A-MR	5	$2.5^\circ \times 1.26^\circ$
	IPSL-CM6A-LR	6	$2.5^\circ \times 1.25^\circ$

To estimate the radiative effects of the DCC, we use the metrics of the DCCRE [6]. The radiative flux at the top of the atmosphere,  $R$ , can be split into the contribution due to

the mean cloud fraction,  $R_0$ , and due to the DCC components. Therefore, we can express the radiative effects of DCC as

$$\text{DCCRE} = R - R_0, \quad (1)$$

where  $R$  is net radiative flux at the top of the atmosphere (TOA) and  $R_0$  is the flux if the cloud fraction was held to its daily mean value. The net radiative flux,  $R$ , can be expressed as two parts for cloudy and clear sky as

$$R = fR_{\text{cld}} + (1 - f)R_{\text{clr}}, \quad (2)$$

where  $R_{\text{cld}}$  and  $R_{\text{clr}}$  are net radiative flux for cloudy and clear sky. The corresponding  $R_0$  can be expressed as

$$R_0 = f_0R_{\text{cld}} + (1 - f_0)R_{\text{clr}}, \quad (3)$$

To link the DCCRE to the CRE, we also need the definition of CRE, i.e.,

$$\text{CRE} = R - R_{\text{clr}}, \quad (4)$$

To find the expression for the DCCRE, we need to substitute Equation (2) into (4),

$$\text{CRE} = f(R_{\text{cld}} - R_{\text{clr}}), \quad (5)$$

Substituting Equations (2) and (3) into (1) yields

$$\text{DCCRE} = (f - f_0)(R_{\text{cld}} - R_{\text{clr}}), \quad (6)$$

Equations (5) and (6) provide the direct relationship between the DCCRE and CRE. Substituting Equation (6) into (5) yields

$$\text{DCCRE} = \frac{f - f_0}{f} \text{CRE}, \quad (7)$$

which is the expression for the DCCRE, where  $f$  is the diurnal cycle of cloud fraction climatology for a given local time and  $f_0$  is the mean cloud fraction. To check if every term adds up correctly, we provide an example with the typical diurnal cycle of the CRE and  $f$  (see Figures 1a and 2 in reference [6]). It is found that the daily averages of the DCCRE, CRE, and  $(f_0/f)\text{CRE}$  are  $-0.49$ ,  $-14.05$ , and  $-13.56 \text{ Wm}^{-2}$ , respectively, explaining the relationship among the DCC, DCCRE, and CRE as stated in Equation (7).

This index essentially separates the DCC radiative effects from the total effects. To calculate the DCCRE, we need sub-daily radiative fluxes at the top of the atmosphere (TOA) under all-sky and clear-sky conditions, which are not available in CMIP5 and only partially available in CMIP6. For this reason, we used hourly TOA radiative fluxes from Clouds and the Earth's Radiant Energy System (CERES) SYN1deg. '(CERES)SYN1deg' is part of the CERES datasets. Synoptic TOA and surface fluxes and clouds (SYN) provide hourly gridded observed TOA and Fu-Liou radiative transfer surface fluxes and clouds. Therefore, the DCCRE evaluated here approximately represents the radiative effects of DCC variations and cannot identify the contribution from diurnal variations of CREs in the corresponding models. While this is similar in spirit to the use of standard radiative kernels in the assessment of the cloud feedback [22], it may involve biases due to inter-model differences in surface albedo, atmospheric temperature, humidity, and aerosols. Therefore, the comparison of the DCCRE and its changes between CMIP5 and CMIP6 should be interpreted with caution. To compare the DCCRE with the CRE, we also used the monthly TOA radiative fluxes under all-sky and clear-sky conditions (variable names: rlut, rlutcs, rsut, rsutcs, see Abbreviations).

We compared climate model outputs with satellite products of the International Satellite Cloud Climatology Project (ISCCP) [23]. It is one of the primary observational data sources available for DCC at global coverage, using infrared band to estimate DCC as it is

measured throughout the whole diurnal cycle (e.g., [6,7,24]). The infrared channel of the ISCCP records and consistently provides 3-hourly cloud fraction products over the whole day covering the globe with 280 km equal-area grids. To make a proper comparison among various climate models and satellite products, we resampled all climate model outputs into 280 km equal-area grids. We focused on the DCC in 2001–2005, covering a period commonly available for all data sources. The DCC evaluated from this relatively short period is consistent with the results of DCC climatology [5], justifying our choice of period for multi-source comparison.

To systematically quantify the DCC, we estimated the cloud fraction climatology at the specific local time of the day,  $f(t)$ , where  $0 < t < 24$  h is the local time of the day. Such a DCC can be calculated for each month to identify its seasonal variations. Particularly, we focused on the phase of the DCC, which can be quantified as the centroid of  $f(t)$  in terms of the circular mean [25]

$$c = \frac{\tau}{2\pi} \arg \int_0^\tau f(t) \exp\left(\mathbf{i} \frac{2\pi t}{\tau}\right) dt, \quad (8)$$

where  $\tau = 24$  h is the period of the whole diurnal cycle,  $\mathbf{i}$  is the imaginary unit, and the operator 'arg' is the argument of any complex number.

With the calculated DCC, we also explored the similarity of DCCs among different sources of data. This is attempted by decomposing the distribution of centroid using principal component analysis (PCA), which is efficient at data compression and has been extensively used in climate studies to identify the important spatial patterns of climate variability [26]. We grouped all centroid data from different data sources into a matrix of  $C$  of  $n \times m$ , where  $n$  is the size of the data sources (i.e., number of climate models) and  $m$  is the size of the interpolated grid points (i.e., 6596 for the 280 km equal-area grid). We decompose  $C$  into

$$CP = T + E, \quad (9)$$

where  $T$  is a  $n \times p$  score matrix,  $P$  is a  $m \times p$  loading matrix,  $p$  is the number of reserved components, and  $E$  is the error term. This composition reduces the dimension from  $n$  global grids to the first few components of  $p$ , allowing us to identify the most prominent spatial patterns of the global DCC.

### 3. Results and Discussion

#### 3.1. Regional Comparisons

We started with the DCC comparison on typical climate zones over the land [27] and another ocean region near the eastern Pacific associated with cloud-feedback hotspots [28]. The East Pacific has large inter-model differences in cloud feedback over the ocean [29] (see the red rectangle box in Figure 1), whereas the three climate zones cross different latitudes over the world, including tropical rain forest (Af), temperate zone (Cwa), and cold zone (Dfb). These regions have been extensively studied in the literature with satellite products or ground observations to investigate their diurnal cycle of clouds or precipitation. We focused on boreal summer (June, July, and August) for these northern and tropical regions where the DCC is expected to have stronger amplitude [5,7]; a more comprehensive analysis for all seasons was conducted at the global scale in Section 3.2.

As the largest rainforest on our planet, precipitation in the Amazon region is largely controlled by changes in the Intertropical Convergence Zone (ITCZ) [30]. While being over the land, the corresponding DCC is quite similar to these in the ITCZ over the ocean where clouds usually peak around midnight from ISCCP [5] and from TRMM with mesoscale convective systems rainfall [31]. For climate models, clouds peak at midnight in CMIP5 but at around 6 a.m. in the early morning in all CMIP6 models, resulting in larger DCC biases. This is consistent with the changes in precipitation, which show increased biases from CMIP5 to CMIP6, particularly near the west coast of the Amazon rainforest [32].

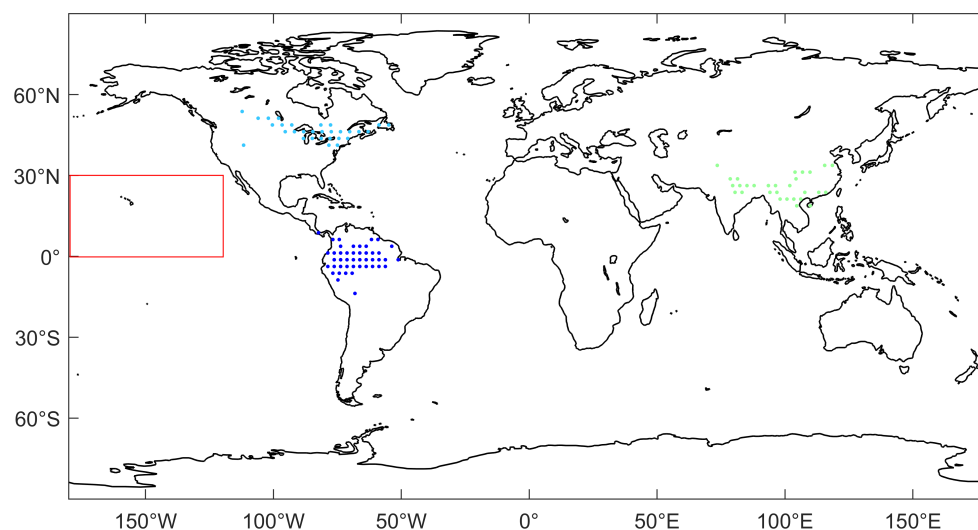


**Figure 1.** Locations for regional comparison of DCC. Three typical climate zones over the land and one region over the ocean were chosen, including the Amazon rainforest (Af, blue dots), southern China (Cwa, green dots), and northern United States (Dfb, cyan dots) across different latitudes over the world and region over the land–atmosphere interaction hotspots in the eastern Pacific (red rectangle).

For the temperate zone near southeastern China, rainfall is associated with the South China Sea monsoon and local circulations, which shows a strong diurnal cycle with peak rainfall occurring at night [33]. However, the summer DCC in this region shows afternoon peaks from satellite products (see Figure 2). This is consistent with observations from rain gauges, which show afternoon rainfall peaks for southeastern China and double rainfall peaks for the southwestern part [34]. Such patterns can be found in climate models with morning cloud peaks for CMCC, FGOALS, and GFDL; afternoon peaks for CNRM; and double peaks for HadGEM and IPSL. Particularly, the afternoon cloud peaks are more visible from CMIP6 for HadGEM models. These inter-model differences may be linked to the difficulties in identifying the contrast patterns of rainfall and clouds across the borders of southeastern and southwestern China.

For cold zones near the border of the United States and Canada, the summer rainfall is often associated with the mesoscale convective systems and is occasionally influenced by tropical cyclones from the south. Similar to the temperate zone near China, midnight rainfall peaks are more frequent in the central and northern United States, whereas afternoon rainfall peaks are often identified in the northeastern United States [35]. From these rainfall patterns, we may also expect two cloud peaks in this cold zone as identified by satellite products with midnight peaks from the ISCCP (see Figure 2). The morning peaks are not evident in the CMCC, CNRM, HadGEM, and IPSL models. Additionally, there are afternoon peaks present in all the climate models. Limited changes were found in cloud peaks from CMIP5 to CMIP6 except for GFDL, which tends to shift the cloud peaks from morning to midday.

Cloud patterns in the eastern Pacific are typically associated with variations in sea surface temperature and surface wind anomalies [36]. It has been discovered that rainfall in this region often peaks at midnight or in the early morning [37]. This is, in general, consistent with cloud patterns from satellite products and all climate model outputs. The former shows that clouds peak around 3 a.m. with larger amplitude, whereas the latter has cloud peaks around 3–6 a.m. Compared with CMIP5, the latest CMIP6 models tend to have smaller DCC amplitudes.

From these regional analyses, we identified typical DCC patterns with midnight cloud peaks over the ocean or regions strongly influenced by large-scale circulation (e.g., ITCZ) and morning and/or afternoon cloud peaks over the land. The DCC over land may have contrasting patterns over some specific borders, thus complicating the DCC simulations

and possibly resulting in large inter-model differences of DCC in climate models. The DCC patterns are often consistent with the patterns of the diurnal cycle of precipitation (DCP), although the exact timing of cloud or precipitation peaking is not necessarily the same. For climate models, we found that there are indeed certain changes in the DCC from CMIP5 to CMIP6, which are consistent with the corresponding changes in the DCP.

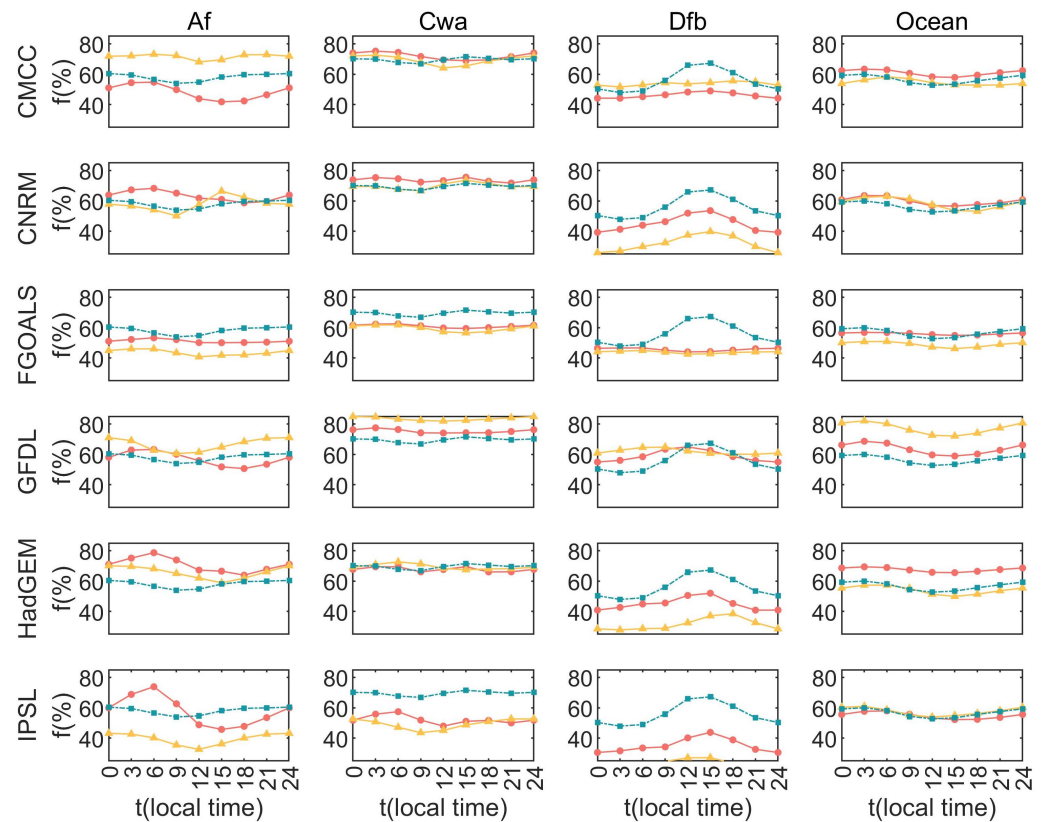


**Figure 2.** Diurnal cloud cycle climatology in boreal summer (June, July, August) during 2001–2005 over the eastern Pacific and three typical climate zones over the land from CMIP5 (▲), CMIP6 (●), and ISCCP (■).

### 3.2. Global Distribution of DCC

The regional comparison in Section 3.1 offers us a detailed description of the DCC for specific areas and shows contrast differences between land and ocean. To explore these patterns at the global scale, we used PCA to decompose the DCC centroid from all climate model outputs (see Section 2). Nearly half of the spatial variability can be explained by the first three components. Particularly, the first component shows clear land/ocean differences (Figure 3). It is, therefore, necessary to separately conduct statistical analyses of the DCC for land and ocean as shown in Figures 4 and 5.

Over the land (see Figure 4), satellite products show that afternoon cloud peaking is the dominant form of the DCC patterns. This feature is not captured in either CMIP5 and CMIP6, which show dominant patterns of morning cloud peaks. Overall, cloud peaks tend to shift earlier in the CMCC, CNRM, FGOALS, and HadGEM models from CMIP5 to CMIP6. Specifically, for CNRM-CM5, cloud peaks are near noon but shift back to early morning in the latest version of CNRM-CM6. These systematical biases of early cloud peaks over the land are consistent with the infrequent occurrences of afternoon convective rainfall events, which exist for both CMIP5 in CMIP6 [38].

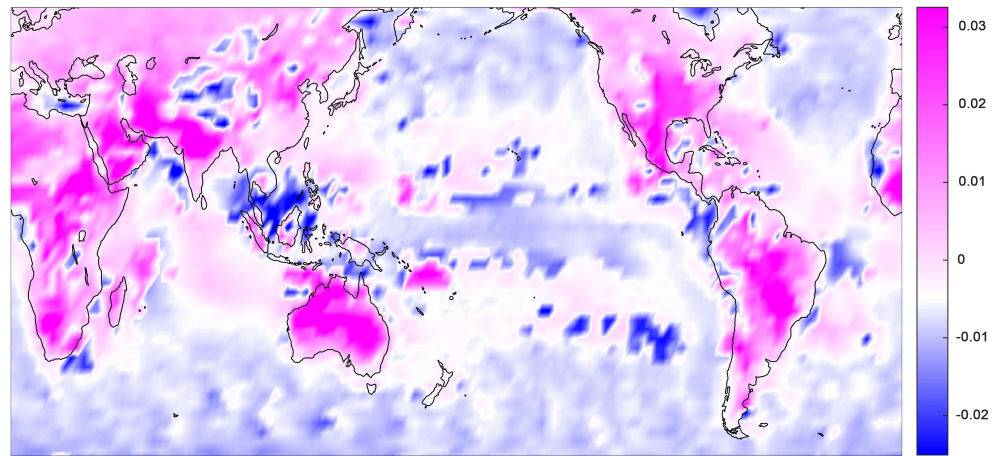


**Figure 3.** First Component extracted from PCA of centroids of all GCM outputs.

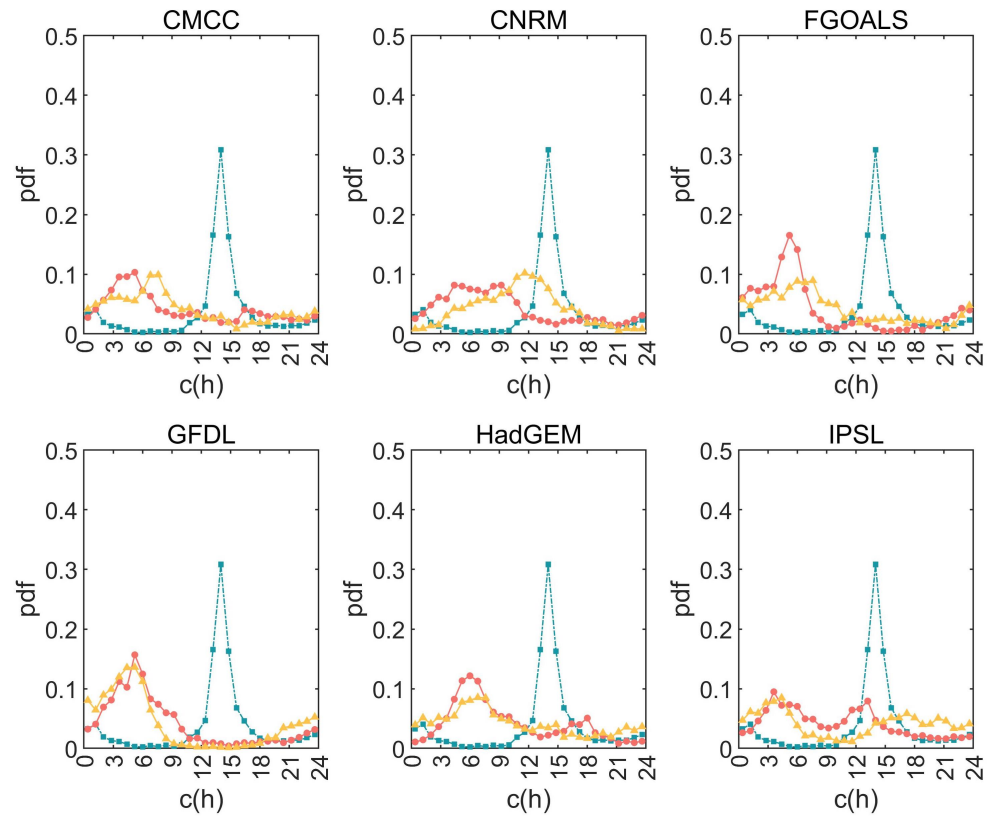


**Figure 4.** Global distribution of DCC centroid over the land. The probability density function (PDF) of  $c$  (centroid of DCC) are estimated for all seasons during 2001–2005 from CMIP5 ( $\blacktriangle$ ), CMIP6 ( $\bullet$ ), and ISCCP ( $\blacksquare$ ).

Over the ocean (see Figure 5), there are significant changes in DCC with clouds peaking after midnight from all climate models and the ISCCP satellite data. For climate model outputs, all results show that clouds peak after midnight, consistent with the results from ISCCP. Moreover, the CMCC, CNRM, FGOALS, and HadGEM models, which tend to have earlier cloud peaks over the land (see Figure 4), also have more frequent earlier clouds over the ocean. Similar shifting patterns are also identified in GFDL and IPSL, which tend to have slightly less frequent earlier clouds in CMIP6. Overall, the cloud phase shifts over the land and ocean from CMIP5 to CMIP6 are generally in the same direction and the same order of magnitude. These synchronized shifting patterns may be associated with the unified cloud schemes used in climate models, as briefly discussed in Section 3.3.

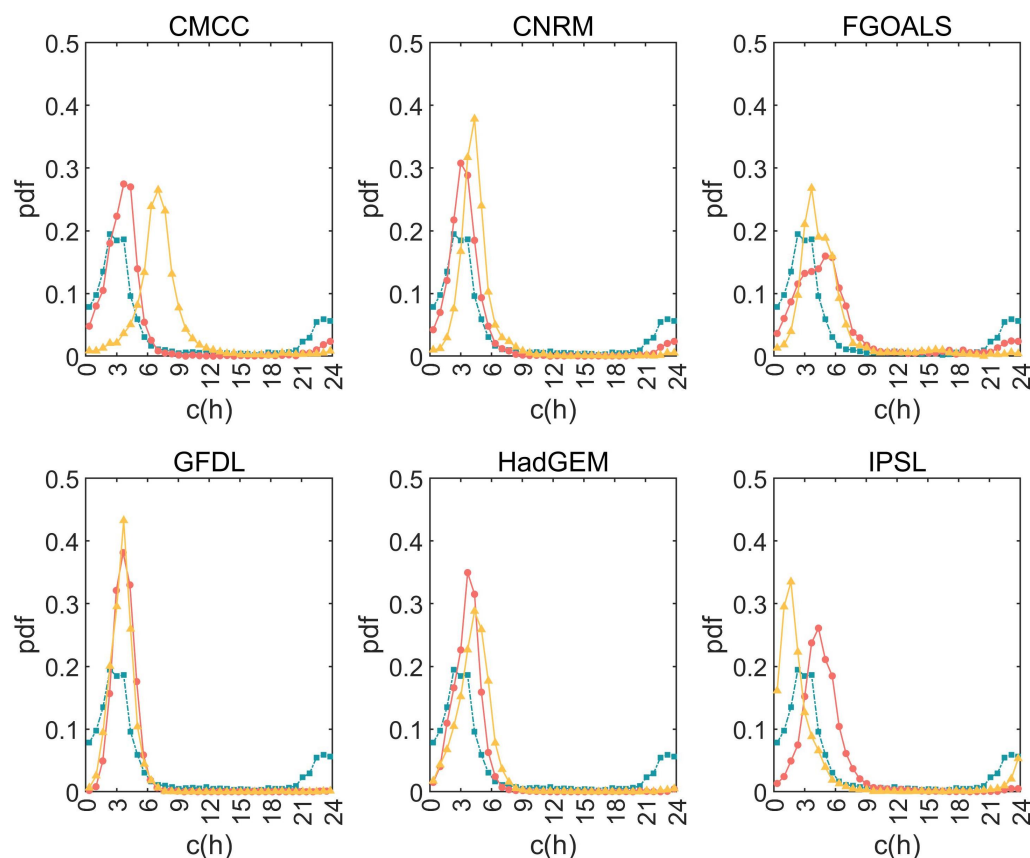


**Figure 5.** As in Figure 4 but for centroids over the ocean.

It should be noted that CMIP6 models aim to improve upon the representations of various components of the Earth system, including clouds, compared to previous model generations. However, the accuracy of cloud simulations in CMIP6 models can vary depending on the specific model and the region or type of clouds being simulated (see Figures 4 and 5). Some CMIP6 models may show improvements in simulating certain aspects of clouds compared to earlier models, while there may still be challenges in accurately representing other aspects such as the DCC explored in this study.

Aside from a direct comparison of cloud simulation, it is also straightforward to use precipitation as a reference variable. Satellite products of global precipitation can be calibrated by rain gauge data [39] and may be alternative references for clouds. It has been shown that rainfall peaks in the latest version of FGOALS move towards midnight over most of the tropics [40], consistent with the results in Figures 4 and 5. However, not all models show similar changes in cloud and precipitation cycles. It is evaluated that the biases of the DCP over land are reduced from CMIP5 to CMIP6 [32], whereas most models show earlier cloud peaks and consequently increase DCC biases. This suggests that precipitation can only be used for diagnosing cloud cycle patterns (e.g., identification of morning or afternoon peaks) but cannot be used to accurately quantify the slight variations associated with model structures (e.g., comparisons between CMIP5 and CMIP6).

### 3.3. Radiative Effects of DCC Variations

With identified differences in the DCC between CMIP5 and CMIP6, one may wonder how these changes could modify the radiation balance modeling and influence climate projections. To address this point, we used Equation (7) and compared the changes in the CRE and DCCRE from CMIP5 to CMIP6 (i.e., noted as  $\Delta$ CRE and  $\Delta$ DCCRE). As shown in Figure 6, the inter-model spreads of  $\Delta$ DCCRE, in terms of standard deviation of the DCCRE changing from CMIP5 to CMIP6, are 0.93, 1.25, and 1.11  $\text{Wm}^{-2}$  over the land, ocean, and globe, respectively, which are nearly half of the spreads of  $\Delta$ CRE, namely 2.90,

2.29, and  $2.33 \text{ Wm}^{-2}$ . As a reference, the radiative forcing of doubling carbon dioxide is estimated to be around  $3.9 \text{ Wm}^{-2}$ . The large spread of  $\Delta\text{DCCRE}$ , when compared with  $\Delta\text{CRE}$ , reveals that a significant portion of the uncertainties in cloud simulations may be associated with the modeling of the DCC.

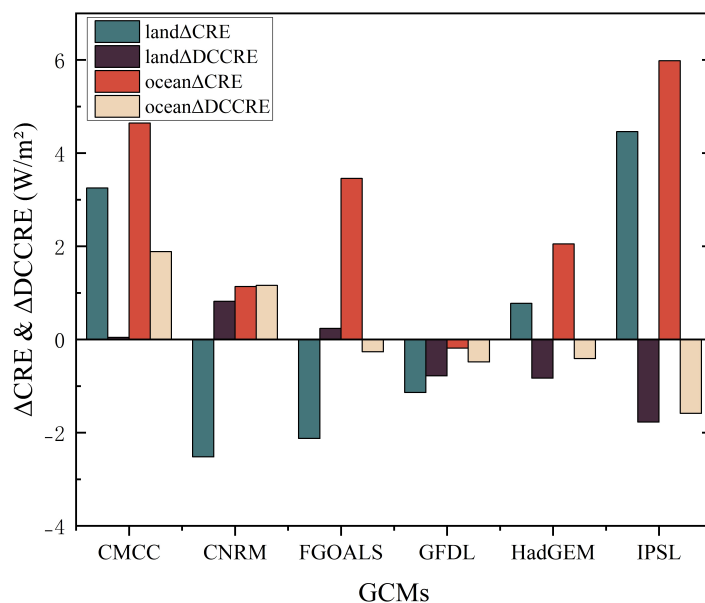


**Figure 6.** Changes in CRE ( $\Delta\text{CRE}$ ) and DCCRE ( $\Delta\text{DCCRE}$ ) from CMIP5 to CMIP6 models.

Moreover, the ensemble mean  $\Delta\text{DCCRE}$  is relatively small, being only  $0.07 \text{ Wm}^{-2}$ , whereas the ensemble mean change in the CRE approaches  $2.15 \text{ Wm}^{-2}$ , which is consistent with other independent studies using a more comprehensive list of models [41]. While the increases in CRE suggest that clouds tend to have relatively warmer effects in the latest climate models than in its earlier versions, no consensus has been reached across different modeling institutes on how to adjust the DCC given its near zero but large spread of  $\Delta\text{DCCRE}$ . With proper calibration from satellite products and in situ observations, this could be a pivotal aspect for improvement in next-generation climate modeling.

To further explore the inter-model differences of the DCC, we group all models based on the first few components of the PCA analysis (see Section 2 and Figure 7), and there are indeed certain changes in the DCC from different generations of climate models except the GFDL and HadGEM models. The term “distances of scores” refers to the distances calculated using the cluster analysis algorithm. These distances serve as indicators of the similarity between different models. Shorter distances between scores indicate higher similarity, while longer distances signify lower similarity. However, CMIP5 and CMIP6 models are not always in the same group, suggesting that there are larger inter-model differences than inter-phase (i.e., in phase 5 or 6) differences. Therefore, it would be interesting to focus on a specific model to explore its changes in the DCC and model structures.

Significant efforts have been made to improve cloud simulation and most models tend to use unified cloud parameterization schemes over both land and ocean. For example, a new shallow convection scheme with revised cloud macrophysics was introduced in CMCC-CM2 [42–45]; continuous and predictive treatment of dry–shallow–deep convection was provided in CNRM-CM6 [46–48]; improved boundary-layer and stratocumulus schemes were used in the second version of MACv2-SP in FGOALS-g3 [49–54]; a double-plume convective closure for shallow and deep convection was developed in GFDL-CM4 [55,56]; a major revision was made to the atmosphere dynamical core and cloud scheme [57]; a statistical triggering for deep convection was introduced in IPSL-CM6A, which integrates the whole process of cloud formation from the first cloud appearance to the deep convection triggering [58–60].

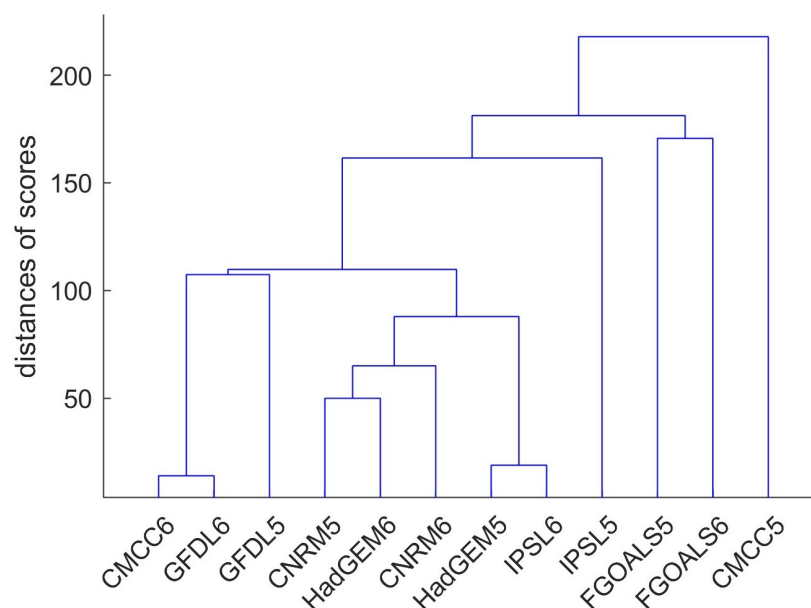


**Figure 7.** Hierarchical clustering of the PCA scores of the first two components, which accounts for 37.7% variability of the centroid data.

The latest climate models tend to have unified cloud schemes, which simulate various cloud types and capture the key factors controlling the transition among dry–moist–deep convection. Such a unified set of parameterizations may be responsible for the synchronized DCC shifting patterns with cloud phase shifting in the same direction and in the same order of magnitude over the land and ocean. Since much larger DCC biases were observed over the land than over the ocean, adjusting the DCC in such unified cloud schemes can only properly reduce the biases either over the ocean or land. If this unified cloud scheme is still used in future climate models, we may expect that it is unlikely to reduce the DCC biases completely.

In this regard, we may need to carefully use the unified cloud schemes and probably integrate different parameterization approaches for land and ocean. Given their contrasting patterns, the DCC should be adjusted separately to slightly shift phase over the ocean but significantly move the cloud peaking time toward the early afternoon over the land. In this way, it is possible to correct the DCC biases at the global scale and reduce their impacts on the modeling of global energy balance.

#### 4. Conclusions

In this study, we conducted comprehensive analyses of sub-daily cloud fraction at both regional and global scales to identify how the diurnal cloud cycle has been changed in the latest updates of climate models. We found that the DCC patterns over land in the Amazon rainforest closely resemble those observed over the ITCZ over the ocean. In the temperate zone of southeastern China and near the cold zone near the border of the United States and Canada, cloud dynamics is associated with large-scale circulation and local convection, and therefore, the clouds peak around afternoon and/or around morning depending on the specific locations. Both cloud peaks were identified from satellite data, while climate models only capture one of these peaks. Over the eastern Pacific region, clouds tend to peak near midnight or early morning from both satellite data and climate model outputs.

At the global scale, we find frequent afternoon cloud peaks from satellite data but morning cloud peaks from climate models over the land; clouds tend to peak at midnight or in the early morning over the ocean from the ISCCP and climate models. The mid-day cloud peaks from CERES may be associated with the artifacts from its geostationary satellite near the Indian Ocean and the northern Pacific. While precipitation can be used as an

alternative variable for identifying the overall DCC patterns, it cannot be used to quantify the small DCC shift associated with the model structure.

From CMIP5 to CMIP6, DCC changes over the land and ocean seem to be synchronized, showing the same shifting direction within the same order of magnitude. Given that much larger DCC biases were observed over the land than over the ocean, such synchronized changes may be inefficient for correcting DCC biases. The inter-model variations of DCC radiative effects are nearly half of these overall cloud changes, hence revealing one of the key cloud features in climate projections.

In conclusion, our study provides valuable insights into the diurnal cloud cycle both within specific climate zones and at the global scale. While advances have been made in understanding and modeling cloud behaviors, our findings underscore the ongoing challenges and the potential for further improvements in capturing the intricacies of the diurnal cloud cycle and its radiative effects in controlling global energy balance.

**Author Contributions:** Conceptualization, Z.J. and J.Y.; methodology, Z.J., Y.A. and J.Y.; software, Z.J.; validation, Z.J.; formal analysis, Z.J., Y.A., and J.Y.; investigation, Z.J. and Y.A.; resources, J.Y.; data curation, Z.J. and Y.A.; writing—original draft preparation, Z.J.; writing—review and editing, Z.J., Y.A., and J.Y.; visualization, Z.J.; supervision, J.Y.; project administration, J.Y.; funding acquisition, J.Y. All authors have read and agreed to the published version of the manuscript.

**Funding:** This research was funded by the Natural Science Foundation of Jiangsu Province (BK20221343) and NUIST startup funding (1441052001003).

**Institutional Review Board Statement:** Not applicable.

**Informed Consent Statement:** Not applicable.

**Data Availability Statement:** ISCCP products are available from <https://isccp.giss.nasa.gov/products/products.html>; CMIP5 and CMIP6 climate model outputs are available at <https://aims2.llnl.gov/search/cmip5/> and <https://aims2.llnl.gov/search/cmip6/>; CERES datasets are available at <https://ceres.larc.nasa.gov/data/>.

**Acknowledgments:** We acknowledge support from NUIST's supercomputing center.

**Conflicts of Interest:** The authors declare no conflicts of interest.

## Abbreviations

The following abbreviations are used in this manuscript:

DCC	Diurnal cloud cycle
CRE	Cloud radiative effects
DCCRE	Diurnal cloud cycle radiative effects
rlut	TOA outgoing longwave radiative flux ( $Wm^{-2}$ )
rlutcs	TOA outgoing clear-sky longwave radiative flux ( $Wm^{-2}$ )
rsut	TOA outgoing shortwave radiative flux ( $Wm^{-2}$ )
rsutcs	TOA outgoing clear-sky shortwave radiative flux ( $Wm^{-2}$ )

## References

- Norris, J.R.; Allen, R.J.; Evan, A.T.; Zelinka, M.D.; O'Dell, C.W.; Klein, S.A. Evidence for climate change in the satellite cloud record. *Nature* **2016**, *536*, 72–75. [[CrossRef](#)]
- Masson-Delmotte, V.; Zhai, P.; Pirani, A.; Connors, S.L.; Péan, C.; Berger, S.; Caud, N.; Chen, Y.; Goldfarb, L.; Gomis, M.; et al. *Climate Change 2021: The Physical Science Basis. Contribution of Working Group I to the Sixth Assessment Report of the Intergovernmental Panel on Climate Change*; Cambridge University Press: Cambridge, UK, 2021; Volume 2.
- Boucher, O.; Randall, D.; Artaxo, P.; Bretherton, C.; Feingold, G.; Forster, P.; Kerminen, V.M.; Kondo, Y.; Liao, H.; Lohmann, U.; et al. Clouds and aerosols. In *Climate Change 2013: The Physical Science Basis. Contribution of Working Group I to the Fifth Assessment Report of the Intergovernmental Panel on Climate Change*; Cambridge University Press: Cambridge, UK, 2013; pp. 571–657.
- Stephens, G.L. Cloud feedbacks in the climate system: A critical review. *J. Clim.* **2005**, *18*, 237–273. [[CrossRef](#)]
- Yin, J.; Porporato, A. Diurnal cloud cycle biases in climate models. *Nat. Commun.* **2017**, *8*, 2269. [[CrossRef](#)]
- Yin, J.; Porporato, A. Radiative effects of daily cycle of cloud frequency in past and future climates. *Clim. Dyn.* **2020**, *54*, 1625–1637. [[CrossRef](#)]

7. Chen, G.; Wang, W.C.; Bao, Q.; Li, J. Evaluation of simulated cloud diurnal variation in CMIP6 climate models. *J. Geophys. Res. Atmos.* **2022**, *127*, e2021JD036422. [[CrossRef](#)]
8. Wu, R.; Chen, G.; Luo, Z.J. Strong Coupling in Diurnal Variations of Clouds, Radiation, Winds, and Precipitation during the East Asian Summer Monsoon. *J. Clim.* **2023**, *36*, 1347–1368. [[CrossRef](#)]
9. Emanuel, K.A. *Atmospheric Convection*; Oxford University Press on Demand: Oxford, UK, 1994.
10. Zhang, Y.; Klein, S.A. Mechanisms affecting the transition from shallow to deep convection over land: Inferences from observations of the diurnal cycle collected at the ARM Southern Great Plains site. *J. Atmos. Sci.* **2010**, *67*, 2943–2959. [[CrossRef](#)]
11. Yin, J.; Albertson, J.D.; Porporato, A. A probabilistic description of entrainment instability for cloud-topped boundary-layer models. *Q. J. R. Meteorol. Soc.* **2017**, *143*, 650–660. [[CrossRef](#)]
12. Gentine, P.; Massmann, A.; Lintner, B.R.; Hamed Alemohammad, S.; Fu, R.; Green, J.K.; Kennedy, D.; Vilà-Guerau de Arellano, J. Land–atmosphere interactions in the tropics—A review. *Hydrol. Earth Syst. Sci.* **2019**, *23*, 4171–4197. [[CrossRef](#)]
13. Wang, Z.; Ge, J.; Yan, J.; Li, W.; Yang, X.; Wang, M.; Hu, X. Interannual shift of tropical high cloud diurnal cycle under global warming. *Clim. Dyn.* **2022**, *59*, 3391–3400. [[CrossRef](#)]
14. Mitchell, D.M.; Lo, Y.T.E.; Seviour, W.J.M.; Haimberger, L.; Polvani, L.M. The vertical profile of recent tropical temperature trends: Persistent model biases in the context of internal variability. *Environ. Res. Lett.* **2020**, *15*, 1040b4. [[CrossRef](#)]
15. Ek, M.; Mahrt, L. Daytime evolution of relative humidity at the boundary layer top. *Mon. Weather Rev.* **1994**, *122*, 2709–2721. [[CrossRef](#)]
16. Yin, J.; Albertson, J.D.; Rigby, J.R.; Porporato, A. Land and atmospheric controls on initiation and intensity of moist convection: CAPE dynamics and LCL crossings. *Water Resour. Res.* **2015**, *51*, 8476–8493. [[CrossRef](#)]
17. Newman, M.; Alexander, M.A.; Ault, T.R.; Cobb, K.M.; Deser, C.; Di Lorenzo, E.; Mantua, N.J.; Miller, A.J.; Minobe, S.; Nakamura, H.; et al. The Pacific decadal oscillation, revisited. *J. Clim.* **2016**, *29*, 4399–4427. [[CrossRef](#)]
18. Meehl, G.A.; Senior, C.A.; Eyring, V.; Flato, G.; Lamarque, J.F.; Stouffer, R.J.; Taylor, K.E.; Schlund, M. Context for interpreting equilibrium climate sensitivity and transient climate response from the CMIP6 Earth system models. *Sci. Adv.* **2020**, *6*, eaba1981. [[CrossRef](#)] [[PubMed](#)]
19. Zelinka, M.D.; Myers, T.A.; McCoy, D.T.; Po-Chedley, S.; Caldwell, P.M.; Ceppi, P.; Klein, S.A.; Taylor, K.E. Causes of Higher Climate Sensitivity in CMIP6 Models. *Geophys. Res. Lett.* **2020**, *47*, e2019GL085782. [[CrossRef](#)]
20. Schiro, K.A.; Su, H.; Ahmed, F.; Dai, N.; Singer, C.E.; Gentine, P.; Elsaesser, G.S.; Jiang, J.H.; Choi, Y.S.; David Neelin, J. Model spread in tropical low cloud feedback tied to overturning circulation response to warming. *Nat. Commun.* **2022**, *13*, 7119. [[CrossRef](#)] [[PubMed](#)]
21. Eyring, V.; Bony, S.; Meehl, G.A.; Senior, C.A.; Stevens, B.; Stouffer, R.J.; Taylor, K.E. Overview of the Coupled Model Intercomparison Project Phase 6 (CMIP6) experimental design and organization. *Geosci. Model Dev.* **2016**, *9*, 1937–1958. [[CrossRef](#)]
22. Soden, B.J.; Held, I.M.; Colman, R.; Shell, K.M.; Kiehl, J.T.; Shields, C.A. Quantifying climate feedbacks using radiative kernels. *J. Clim.* **2008**, *21*, 3504–3520. [[CrossRef](#)]
23. Doelling, D.R.; Sun, M.; Nordeen, M.L.; Haney, C.O.; Keyes, D.F.; Mlynczak, P.E. Advances in geostationary-derived longwave fluxes for the CERES synoptic (SYN1deg) product. *J. Atmos. Ocean. Technol.* **2016**, *33*, 503–521. [[CrossRef](#)]
24. Bergman, J.W.; Salby, M.L. The role of cloud diurnal variations in the time-mean energy budget. *J. Clim.* **1997**, *10*, 1114–1124. [[CrossRef](#)]
25. Jammalamadaka, S.R.; Sengupta, A. *Topics in Circular Statistics*; World Scientific: Singapore, 2001; Volume 5.
26. Jolliffe, I.T.; Cadima, J. Principal component analysis: A review and recent developments. *Philos. Trans. R. Soc. A Math. Phys. Eng. Sci.* **2016**, *374*, 20150202. [[CrossRef](#)]
27. Beck, H.E.; Zimmermann, N.E.; McVicar, T.R.; Vergopolan, N.; Berg, A.; Wood, E.F. Present and future Köppen-Geiger climate classification maps at 1-km resolution. *Sci. Data* **2018**, *5*, 180214. [[CrossRef](#)] [[PubMed](#)]
28. Webb, M.J.; Andrews, T.; Bodas-Salcedo, A.; Bony, S.; Bretherton, C.S.; Chadwick, R.; Chepfer, H.; Douville, H.; Good, P.; Kay, J.E.; et al. The cloud feedback model intercomparison project (CFMIP) contribution to CMIP6. *Geosci. Model Dev.* **2017**, *10*, 359–384. [[CrossRef](#)]
29. Bony, S.; Webb, M.; Bretherton, C.; Klein, S.; Siebesma, P.; Tselioudis, G.; Zhang, M. CFMIP: Towards a better evaluation and understanding of clouds and cloud feedbacks in CMIP5 models. *Clivar Exch.* **2011**, *56*, 20–22.
30. Schneider, T.; Bischoff, T.; Haug, G.H. Migrations and dynamics of the intertropical convergence zone. *Nature* **2014**, *513*, 45–53. [[CrossRef](#)] [[PubMed](#)]
31. Nesbitt, S.W.; Zipser, E.J. The diurnal cycle of rainfall and convective intensity according to three years of TRMM measurements. *J. Clim.* **2003**, *16*, 1456–1475. [[CrossRef](#)]
32. Lee, Y.C.; Wang, Y.C. Evaluating Diurnal Rainfall Signal Performance from CMIP5 to CMIP6. *J. Clim.* **2021**, *34*, 7607–7623. [[CrossRef](#)]
33. Bai, L.; Chen, G.; Huang, L. Convection Initiation in Monsoon Coastal Areas (South China). *Geophys. Res. Lett.* **2020**, *47*. [[CrossRef](#)]
34. Li, J.; Yu, R.; Zhou, T. Seasonal Variation of the Diurnal Cycle of Rainfall in Southern Contiguous China. *J. Clim.* **2008**, *21*, 6036–6043. [[CrossRef](#)]
35. Li, X.; Lu, R.; Wang, X. Effect of Large-scale Circulation Anomalies on Summer Rainfall over the Yangtze River Basin: Tropical versus Extratropical. *J. Clim.* **2023**, *36*, 4571–4587. [[CrossRef](#)]

36. Deser, C.; Wallace, J.M. Large-Scale Atmospheric Circulation Features of Warm and Cold Episodes in the Tropical Pacific. *J. Clim.* **1990**, *3*, 1254–1281. [[CrossRef](#)]
37. Watters, D.; Battaglia, A.; Allan, R.P. The Diurnal Cycle of Precipitation according to Multiple Decades of Global Satellite Observations, Three CMIP6 Models, and the ECMWF Reanalysis. *J. Clim.* **2021**, *34*, 5063–5080. [[CrossRef](#)]
38. Christopoulos, C.; Schneider, T. Assessing biases and climate implications of the diurnal precipitation cycle in climate models. *Geophys. Res. Lett.* **2021**, *48*, e2021GL093017. [[CrossRef](#)]
39. Sun, Q.; Miao, C.; Duan, Q.; Ashouri, H.; Sorooshian, S.; Hsu, K.L. A review of global precipitation data sets: Data sources, estimation, and intercomparisons. *Rev. Geophys.* **2018**, *56*, 79–107. [[CrossRef](#)]
40. Tang, S.; Gleckler, P.; Xie, S.; Lee, J.; Ahn, M.S.; Covey, C.; Zhang, C. Evaluating the diurnal and semidiurnal cycle of precipitation in CMIP6 models using satellite-and ground-based observations. *J. Clim.* **2021**, *34*, 3189–3210.
41. Wild, M. The global energy balance as represented in CMIP6 climate models. *Clim. Dyn.* **2020**, *55*, 553–577. [[CrossRef](#)]
42. Cherchi, A.; Fogli, P.G.; Lovato, T.; Peano, D.; Iovino, D.; Gualdi, S.; Masina, S.; Scoccimarro, E.; Materia, S.; Bellucci, A.; et al. Global mean climate and main patterns of variability in the CMCC-CM2 coupled model. *J. Adv. Model. Earth Syst.* **2019**, *11*, 185–209. [[CrossRef](#)]
43. Park, S.; Bretherton, C.S. The University of Washington shallow convection and moist turbulence schemes and their impact on climate simulations with the Community Atmosphere Model. *J. Clim.* **2009**, *22*, 3449–3469. [[CrossRef](#)]
44. Park, S.; Bretherton, C.S.; Rasch, P.J. Integrating cloud processes in the Community Atmosphere Model, version 5. *J. Clim.* **2014**, *27*, 6821–6856. [[CrossRef](#)]
45. Iacono, M.J.; Delamere, J.S.; Mlawer, E.J.; Shephard, M.W.; Clough, S.A.; Collins, W.D. Radiative forcing by long-lived greenhouse gases: Calculations with the AER radiative transfer models. *J. Geophys. Res. Atmos.* **2008**, *113*. [[CrossRef](#)]
46. Voldoire, A.; Saint-Martin, D.; Sénéci, S.; Decharme, B.; Alias, A.; Chevallier, M.; Colin, J.; Guérémy, J.F.; Michou, M.; Moine, M.P.; et al. Evaluation of CMIP6 deck experiments with CNRM-CM6-1. *J. Adv. Model. Earth Syst.* **2019**, *11*, 2177–2213. [[CrossRef](#)]
47. Guérémy, J. A continuous buoyancy based convection scheme: One-and three-dimensional validation. *Tellus A Dyn. Meteorol. Oceanogr.* **2011**, *63*, 687–706. [[CrossRef](#)]
48. Piriou, J.M.; Redelsperger, J.L.; Geleyn, J.F.; Lafore, J.P.; Guichard, F. An approach for convective parameterization with memory: Separating microphysics and transport in grid-scale equations. *J. Atmos. Sci.* **2007**, *64*, 4127–4139. [[CrossRef](#)]
49. Li, L.; Yu, Y.; Tang, Y.; Lin, P.; Xie, J.; Song, M.; Dong, L.; Zhou, T.; Liu, L.; Wang, L.; et al. The flexible global ocean-atmosphere-land system model grid-point version 3 (FGOALS-g3): Description and evaluation. *J. Adv. Model. Earth Syst.* **2020**, *12*, e2019MS002012. [[CrossRef](#)]
50. Wu, X.; Deng, L.; Song, X.; Zhang, G.J. Coupling of convective momentum transport with convective heating in global climate simulations. *J. Atmos. Sci.* **2007**, *64*, 1334–1349. [[CrossRef](#)]
51. Guo, Z.; Zhou, T. An improved diagnostic stratocumulus scheme based on estimated inversion strength and its performance in GAMIL2. *Sci. China Earth Sci.* **2014**, *57*, 2637–2649. [[CrossRef](#)]
52. Shi, X.; Zhang, W.; Liu, J. Comparison of anthropogenic aerosol climate effects among three climate models with reduced complexity. *Atmosphere* **2019**, *10*, 456. [[CrossRef](#)]
53. Stevens, B.; Fiedler, S.; Kinne, S.; Peters, K.; Rast, S.; Müssé, J.; Smith, S.J.; Mauritsen, T. MACv2-SP: A parameterization of anthropogenic aerosol optical properties and an associated Twomey effect for use in CMIP6. *Geosci. Model Dev.* **2017**, *10*, 433–452. [[CrossRef](#)]
54. Sun, W.; Li, L.; Wang, B. Reducing the biases in shortwave cloud radiative forcing in tropical and subtropical regions from the perspective of boundary layer processes. *Sci. China Earth Sci.* **2016**, *59*, 1427–1439. [[CrossRef](#)]
55. Zhao, M.; Golaz, J.C.; Held, I.; Guo, H.; Balaji, V.; Benson, R.; Chen, J.H.; Chen, X.; Donner, L.; Dunne, J.; et al. The GFDL global atmosphere and land model AM4. 0/LM4. 0: 1. Simulation characteristics with prescribed SSTs. *J. Adv. Model. Earth Syst.* **2018**, *10*, 691–734. [[CrossRef](#)]
56. Zhao, M.; Golaz, J.C.; Held, I.; Guo, H.; Balaji, V.; Benson, R.; Chen, J.H.; Chen, X.; Donner, L.; Dunne, J.; et al. The GFDL global atmosphere and land model AM4. 0/LM4. 0: 2. Model description, sensitivity studies, and tuning strategies. *J. Adv. Model. Earth Syst.* **2018**, *10*, 735–769. [[CrossRef](#)]
57. Williams, K.; Copesey, D.; Blockley, E.; Bodas-Salcedo, A.; Calvert, D.; Comer, R.; Davis, P.; Graham, T.; Hewitt, H.; Hill, R.; et al. The Met Office global coupled model 3.0 and 3.1 (GC3. 0 and GC3. 1) configurations. *J. Adv. Model. Earth Syst.* **2018**, *10*, 357–380. [[CrossRef](#)]
58. Hourdin, F.; Jam, A.; Rio, C.; Couvreur, F.; Sandu, I.; Lefebvre, M.P.; Brient, F.; Idelkadi, A. Unified parameterization of convective boundary layer transport and clouds with the thermal plume model. *J. Adv. Model. Earth Syst.* **2019**, *11*, 2910–2933. [[CrossRef](#)]
59. Rochetin, N.; Couvreur, F.; Grandpeix, J.Y.; Rio, C. Deep convection triggering by boundary layer thermals. Part I: LES analysis and stochastic triggering formulation. *J. Atmos. Sci.* **2014**, *71*, 496–514. [[CrossRef](#)]
60. Rochetin, N.; Grandpeix, J.Y.; Rio, C.; Couvreur, F. Deep convection triggering by boundary layer thermals. Part II: Stochastic triggering parameterization for the LMDZ GCM. *J. Atmos. Sci.* **2014**, *71*, 515–538. [[CrossRef](#)]

**Disclaimer/Publisher’s Note:** The statements, opinions and data contained in all publications are solely those of the individual author(s) and contributor(s) and not of MDPI and/or the editor(s). MDPI and/or the editor(s) disclaim responsibility for any injury to people or property resulting from any ideas, methods, instructions or products referred to in the content.